Gao, N., Geyer, F., Pilat, D. W., Wooh, S., Vollmer, D., Butt, H.-J., et al. (2018). How drops start sliding over solid surfaces. Nature Physics, 14(2), 191-196. doi:10.1038/NPHYS4305.

, which has been published in final form at: 10.1038/NPHYS4305

How drops start sliding over solid surfaces

Nan Gao, Florian Geyer, Dominik W. Pilat, Sanghyuk Wooh, Doris Vollmer, Hans-Jürgen Butt & Rüdiger Berger

How drops start sliding over solid surfaces

Nan Gao[1,2*], Florian Geyer[1], Dominik W. Pilat[1], Sanghyuk Wooh[1], Doris Vollmer[1], Hans-Jürgen Butt[1], Rüdiger Berger[1*]

1 Max Planck Institute for Polymer Research, Ackermannweg 10, 55128 Mainz, Germany

2 Fudan University, 220 Handan Road, Shanghai 200433, People's Republic of China

* Email: nann.gao@gmail.com

* Email: berger@mpip-mainz.mpg.de

It has been known for more than 200 years that the maximum static friction force between two solid surfaces is usually greater than the kinetic friction force. In contrast to solid–solid friction, there is a lack of understanding of liquid–solid friction, i.e. the forces that impede the lateral motion of a drop of liquid on a solid surface. Here, we report that the lateral adhesion force between a liquid drop and a solid can be divided into a static and a kinetic regime. This striking analogy with solid–solid friction is a generic phenomenon that holds for liquids of different polarities and surface tensions on smooth, rough and structured surfaces.

When two solid objects are brought into contact, a threshold force F_{THRD} must be overcome in order for one of the objects to slide[1-3]. This phenomenon can be visualised in a typical classroom experiment where a solid block attached to a spring is pulled over a solid surface (Fig. 1a). The static force F_{S} is applied to the stationary block and then increased until it exceeds F_{THRD}, upon which the block begins to slide. After that, a lower kinetic force F_{KIN} is required to maintain the block's motion[3]. However, it is not clear whether these forces develop in a comparable manner when a drop of liquid resting on a solid surface starts to slide. This gap in our understanding is astonishing, given the fact that liquid drops are omnipresent in our lives and their motion is relevant for numerous applications, including microfluidics[4], printing[5], condensation[6,7], and water collection[8,9]. Hence insight on the behaviour of drops that start sliding over solid surfaces is needed.

A sessile drop of liquid is usually in molecular contact with the supporting solid surface. In contrast, two solid bodies are in direct contact only at asperities owing to surface roughness[10,11]. Thus, the real contact area of a solid–solid contact is much smaller than the apparent contact area. Consequently the sliding of drops might be fundamentally different. However, by simply observing a drop of water on a pivot window pane, we know that also sessile drops start sliding when a critical tilt angle is reached, i.e. when the gravitational force acting on the drop overcomes the lateral adhesion force. The question may therefore be raised whether a static and a kinetic regime are also present for sessile drops. The general questions is: How do drops start sliding over solid surfaces and how do the forces develop while the drops slide?

Owing to higher gravitational forces, larger drops start sliding at lower tilt angles. Sliding is opposed by capillary forces. They are associated with a contact angle difference between the rear and the front of the drop. Indeed, the interactions between solid surfaces and liquids are described by the liquid–air surface tension γ and the apparent rear and front contact angles of the drop, θ_{Rear} and θ_{Front}, respectively. Thus, the surface tension, the contact angles and the drop contact width L determine the lateral adhesion force F_{LA} by[12-16]

$$F_{\mathrm{LA}} = k \cdot L \cdot \gamma \cdot (\cos\theta_{\mathrm{Rear}} - \cos\theta_{\mathrm{Front}}). \qquad \text{Eq. (1)}$$

The dimensionless factor k accounts for the precise shape of the solid–liquid–air three-phase contact line of the drop. Values for k were calculated to be between 1/2 and π/2.[12,17-19]

Despite the omnipresence of drops, the onset of motion has never been correlated with the development of lateral adhesion forces. The lateral adhesion force has been related to external forces that cause a drop to slide, such as gravitational[20,21], centrifugal[22], magnetic[23], or capillary forces[24-26]. The contact angles have also been experimentally and numerically investigated for the pinned state, i.e. just before and during steady motions[27,28]. However, once a drop has started to slide, the lateral adhesion force cannot be tracked using simple techniques. Astonishingly, it is unclear how the force develops and how it depends on sliding velocity. We will demonstrate that, for the lateral liquid–solid adhesion, we can distinguish a static and a kinetic regime, analogous to solid–solid friction.

In order to measure the lateral adhesion force between a drop of liquid and a solid substrate, a capillary is positioned in the centre of the drop. The substrate with the drop is moved sideways against the capillary at a constant velocity. When the capillary reaches the edge of the drop, it sticks to the drop. Consequently the motion of the substrate is accompanied by a deformation of the drop as well as a deflection of the capillary. Initially, the drop remains pinned to the substrate (Fig. 1b). Once the capillary exerts a certain critical force, the drop overcomes the lateral adhesion and is set into translational motion relative to the substrate, i.e. the front and rear side of the drop start moving. The deflection D of the capillary is measured by recording the position of a reflected laser beam with a position-sensitive detector [25]. Then, the lateral adhesion force acting on the drop can be calculated by $F_{LA} = \kappa \cdot D$, where κ is the spring constant of the capillary. Simultaneously, the drop’s shape is monitored by two cameras, which are synchronised with the force measurement. In this way the lateral adhesion force can be correlated with the contact angles. Velocities ranged from 1 μm/s to 50 mm/s (see methods section).

As a representative example we start with a drop of an ionic liquid placed on a fluorinated Si wafer. It forms a contact angle of ≈70°. Moving the wafer laterally increased the force (blue circles in Fig. 2a) until a maximum force of 50 μN was reached (after 11 s). This maximum force corresponded to the threshold force for the drop, upon which it started to slide. Then the force subsequently decreased to a constant level of ≈33 μN, which was only 66% of the maximal force (after 17 s). Accordingly, we distinguish a static, a transition, and a kinetic regime shown in different shades of green in Fig. 2a. The presence of a higher threshold force compared to the force required for continuous motion explains the manner a drop slides downhill in a tilted-plate experiment. It is analogous to solid–solid friction, where a solid object placed on a tilted plane keeps sliding once the static friction threshold force has been overcome[29,30]. Initially, the contact line of the drop was pinned and the contact width and length remained constant at about 2.3 mm (Fig. 2b, first 5 s). Meanwhile, the front and rear contact angles increased and decreased, respectively, as the drop deformed (Fig. 2c). After 5 – 8 s, the contact line started reforming, resulting in a longer and narrower drop shape. After about 10 s, the contact angles reached a maximum value of ≈86° at the front and a minimum of ≈43° at the rear. At this point of maximum contact angle difference of ≈40°, the static adhesion force reached its maximum, which constituted the threshold force of the translational motion. In the transition regime, the contact length decreased continuously. The rear contact angle increased by more than 10°, whereas the front contact angle decreased by ≈5° over time. Finally a kinetic regime was reached (after ≈18 s), which was characterized by constant lateral adhesion forces, constant contact angles, constant contact widths and contact lengths.

We then took the measured contact widths (Fig. 2b) and the contact angles (Fig. 2c) to calculate the lateral adhesion force using Eq. 1. Thereby we simplified Eq. 1 by assuming a constant value of $k = 1$ thus disregarding shape changes of the drop contour and variations of the contact angle along the contour[17] (see Supplementary Material for a discussion of the k factor and its temporal development). This calculation almost quantitatively agreed with the measured lateral adhesion force (red squares in Fig. 2a). In particular, the calculated lateral adhesion force reproduced the transition between the static and kinetic regimes. Once the threshold adhesion force F_{THRD} has been overcome, the drop transitions from a static regime to a steady kinetic regime. Consequently, the liquid–solid adhesion forces in the static and kinetic regimes are substantially different, owing to different contact angles and contact widths in these two regimes:

$$F_{\mathrm{S}} = \gamma \cdot L_{\mathrm{S}} \cdot \left(\cos\theta_{S}^{\mathrm{Rear}} - \cos\theta_{S}^{\mathrm{Front}}\right) \qquad \text{(Eq. 2a)}$$

$$F_{\mathrm{KIN}} = \gamma \cdot L_{\mathrm{KIN}} \cdot \left(\cos\theta_{\mathrm{KIN}}^{\mathrm{Rear}} - \cos\theta_{\mathrm{KIN}}^{\mathrm{Front}}\right) \qquad \text{(Eq. 2b)}$$

Here, F_{S}, L_{S}, $\theta_{S}^{\mathrm{Front}}$ and $\theta_{S}^{\mathrm{Rear}}$ are the lateral adhesion force, contact width, and front and rear contact angles in the static (S) regime. F_{KIN}, L_{K}, $\theta_{\mathrm{KIN}}^{\mathrm{Front}}$ and $\theta_{\mathrm{KIN}}^{\mathrm{Rear}}$ are the lateral adhesion force, contact width, and front and rear contact angles in the kinetic (KIN) regime.

To verify whether the discrimination between static and kinetic lateral adhesion forces is a generic feature, we analysed a number of different liquid–solid combinations (Fig. 3). We used water and hexadecane in addition to a non-volatile ionic liquid (1-butyl-2,3-dimethylimidazolium bis(trifluoromethanesulfonyl)imide). The solid surfaces include superhydrophobic silicone nanofilaments (SNFs), silicon wafers (Si), SU-8 micropillar arrays, multilayers of titanium dioxide nanoparticles (TiO_2) and cross-linked polydimethylsiloxane (PDMS) substrates (Supplementary Fig. 1). All samples were homogenous at the scale of the drop radius and did not have distinct pinning centers. For all liquid–solid combinations we observed a static, a transition and a kinetic regime (Fig. 3a, Supplementary Figs. 5-10). It should be noted that the lateral adhesion force in the kinetic regime never exceeded the threshold force (Fig. 3a). Thus

$$F_{\mathrm{THRD}} \geq F_{\mathrm{KIN}} \qquad \text{(Eq. 3)}$$

Notably, $F_{\mathrm{THRD}} = F_{\mathrm{KIN}}$ is possible, too[25]. Surfaces coated with brushes of liquid like poly(dimethylsiloxane) (PDMS) showed $F_{\mathrm{THRD}} = F_{\mathrm{KIN}}$. The reason is that these surfaces hardly show any contact angle hysteresis for water[31], i.e. $cos\theta^{Rear} \approx cos\theta^{Front}$ (Supplementary Fig. 11).

Furthermore, good agreement between calculated and measured lateral adhesion forces was observed for various wetting scenarios, including hexadecane and ionic liquid on fluorinated silicon wafers, and water on superhydrophobic surfaces (silicone nanofilaments and fluorinated SU-8 pillars), where drops partially rested on air cushions. The differences in adhesion between the drops and the substrates resulted in different apparent contact angles and contact widths among the liquid–solid combinations (Supplementary Figs. 5–10). We attribute the small discrepancies between calculated and measured lateral adhesion forces to microscopic distortions of the three-phase contact lines[30]. The latter can be accounted for by the *k* factor (Supplementary Figs. 5-10 and Supplementary Table 1). Indeed, the *k* factor of our measurements lies between 0.25 and 4. It is worth emphasizing that the *k* factor changed continuously while the drop passed from the static to the kinetic regime. These observations indicate that a constant *k* factor is not sufficient to describe how drops slide over a solid surface. In particular for large scale heterogeneous surfaces that exhibit distinct pinning centers, F_{KIN} occasionally exceeded F_{THRD} (Supplementary Fig. 12 and Griffiths et. al.[32]]. Thus, the lateral adhesion force provides quantitative information on the homogeneity or cleanliness of a surface.

In order to compare the different liquid–solid combinations independently from drop size, we calculated the static and lateral adhesion force per unit width (Fig. 3b). This analysis yielded values ranging from 2 μN/mm to 110 μN/mm. The increasing lateral adhesion force per unit width depends on the interplay between surface tension and contact angle hysteresis. In addition, we calculated the ratios of the kinetic force divided by the static threshold force. For all different liquid–solid combinations, we obtained a ratio of $F_{\mathrm{KIN}}/F_{\mathrm{THRD}} \leq 1$ (Fig. 3c).

In general, contact angles depend on the sliding velocity.[33] Therefore we measured F_{KIN} and F_{THRD} for increasing sliding velocities in a velocity range from 10^{-3} to 22 mm/s for hexadecane on a Silicon wafer surface (filled symbols in Fig. 4a-b). We found that F_{KIN} and F_{THRD} are relatively constant up to a Ca of 10^{-5}. Then they increase with velocity. Furthermore, the dependence and magnitude of the measured forces are in agreement with the forces calculated by the front and rear contact angles (Fig. 4c) using equation 1 (open symbols in Fig. 4a-b). Perrin et al. measured the dynamic macroscopic contact angle of a silicon wafer withdrawn from a silicone oil bath[34]. These experiments revealed a strong change in the cosines of the contact angles between $10^{-5} < \mathrm{Ca} < 10^{-3}$. This region marked the transition from energy dissipation dominated by defects to viscous dissipation. Our measured increase in F_{KIN} falls in this regime and therefore we attribute the increase of F_{KIN} at Ca > 10^{-5} to viscous dissipation in addition to thermally activated process at the contact line. The increase in F_{KIN} falls in this regime, and therefore we attribute the increase of F_{KIN} at Ca > 10^{-5} to viscous dissipation in addition to thermally activated processes at the contact line. The latter was discussed as a result of a rugged energy landscape of the sample surface leading to a thermally activated process of the contact line dynamics.[34] In our measurements, we could not resolve a logarithmic dependence of F_{KIN} and F_{THRD} at Ca < 10^{-5} which would have given insight into such thermally activated process of the moving liquid. In particular, we found that the ratio of $F_{\mathrm{KIN}}/F_{\mathrm{THRD}} \leq 1$ within the probed velocity range (Supplementary Figure 13 and 14).

In order to study whether drop-solid friction scales with the contact line or with contact area, we varied the drop volume (Supplementary Fig. 13). This results in a variation of the contact area by a factor of > 4. The linear extrapolation of the kinetic force dependence suggests a linear dependence with an intercept slightly below zero force. Therefore we conclude that the liquid drop friction is dominated by contact line friction and interfacial friction only plays a minor role. This conclusion is supported by an estimation of the friction force contribution of a solid-liquid interface based on a Green-Kubo relation of Huang and Szlufarska[35] and by monitoring the motion of drops over the surfaces, showing that the motion is dominated by rolling (Supplementary Fig. 15, Movies 8-11). In contrast, contact line friction does not play a role for liquid-liquid interfaces such as drops on lubricated surfaces.[36]

As an example of a natural, structured surface, we measured the lateral adhesion of a water drop on a goose feather (Fig. 5). Again, we observed a static regime and a kinetic regime. The static threshold force was even 2.4 times larger than the average kinetic force required for the continuous motion of the water drop. In addition, the lateral adhesion force varied in the kinetic regime (Fig. 5b). Likely, these variations are related to the flexibility and the microscopic structures of the feather (Fig. 5c-d) which lead to a stick-slip motion of the drop. Energy is dissipated mainly by depinning from a few surface protrusions which shows no velocity dependence (Supplementary Fig. 16) [37]. The latter is in contrast to stick-slip motion of two solids.[38,39] Consequently, for such rough and elastic surfaces the contribution of viscous dissipation to the overall energy dissipation of the sliding drop is low. It is not clear what role such a stick-slip motion and the associated velocity independence play for the live of a goose in water. The constant and low kinetic force could potentially reduce energy losses at the three-phase contact line of the feather with water and air.

Acknowledgement

We thank G. Auernhammer, M. Bonn, N. Encinas, M. Kappl, T. Kajiya, P. Papadopoulos, F. Schellenberger, W. Steffen, and D. Wang for simulating discussions, and M. Bach, G. Glaser and G. Schäfer for technical support. This work was supported by the SPP 1420 (H.J. B.), ERC advanced grant 340391–SUPRO and SPP 8173 (D. V.). N.G. thanks the National Postdoctoral Science Foundation of China for the International Postdoctoral Fellowship, and S.W. thanks the Alexander von Humboldt Foundation for a postdoctoral fellowship. D.W.P. is grateful for funding from the German National Academic Foundation.

Author contributions

N.G. carried out the experiments and wrote the manuscript. D.W.P., R.B. and H.-J.B. designed and constructed the homebuilt setup. F.G. and S.W. prepared the solid surfaces. R.B., D.V., N.G. and H.-J.B. contributed to the experimental planning, data analysis, and manuscript preparation. All authors reviewed and approved the manuscript.

Additional information

Supplementary information is available in the online version of this paper. Reprints and permissions information are available online at www……com/reprints. Correspondence and requests for materials should be addressed to R.B., H.-J.B. or D.V.

Data Availability Statement: The data that support the plots within this paper and other findings of this study are available from the corresponding author upon request.

Competing financial interests

The authors declare no competing financial interests.

References

1 Archard, J. F. Contact and Rubbing of Flat Surfaces. *J. Appl. Phys.* **24**, 981-988, (1953).
2 Persson, B. T. in *Encyclopedia of Lubricants and Lubrication* (ed Theo Mang) Ch. 80, 791-797 (Springer Berlin Heidelberg, 2014).
3 Butt, H.-J. & Kappl, M. *Friction*. (Wiley-VCH Verlag GmbH & Co. KGaA, 2010).
4 Shestopalov, I., Tice, J. D. & Ismagilov, R. F. Multi-step synthesis of nanoparticles performed on millisecond time scale in a microfluidic droplet-based system. *Lab Chip* **4**, 316-321, (2004).
5 Calvert, P. Inkjet Printing for Materials and Devices. *Chem. Mater.* **13**, 3299-3305, (2001).
6 Cheng, P., Quan, X., Gong, S., Liu, X. & Yang, L. in *Advances in Heat Transfer* Vol. 46 (eds Young I. Cho John P. Abraham Ephraim M. Sparrow & Gorman John M) 187-248 (Elsevier, 2014).
7 Rykaczewski, K. *et al.* Dropwise Condensation of Low Surface Tension Fluids on Omniphobic Surfaces. *Sci. Rep.* **4**, 4158; DOI:10.1038/srep04158, (2014).

8 Zheng, Y. *et al.* Directional water collection on wetted spider silk. *Nature* **463**, 640-643, (2010).

9 Park, K.-C., Chhatre, S. S., Srinivasan, S., Cohen, R. E. & McKinley, G. H. Optimal Design of Permeable Fiber Network Structures for Fog Harvesting. *Langmuir* **29**, 13269-13277, (2013).

10 Bowden, F. P. & Tabor, D. *The Friction and Lubrication of Solids*. (Clarendon Press, 2001).

11 Bhushan, B., Israelachvili, J. N. & Landman, U. Nanotribology: friction, wear and lubrication at the atomic scale. *Nature* **374**, 607-616, (1995).

12 Extrand, C. W. & Gent, A. N. Retention of liquid drops by solid surfaces. *J. Colloid Interface Sci.* **138**, 431-442, (1990).

13 Brown, R. A., Orr Jr, F. M. & Scriven, L. E. Static drop on an inclined plate: Analysis by the finite element method. *J. Colloid Interface Sci.* **73**, 76-87, (1980).

14 Extrand, C. W. & Kumagai, Y. Liquid Drops on an Inclined Plane: The Relation between Contact Angles, Drop Shape, and Retentive Force. *J. Colloid Interface Sci.* **170**, 515-521, (1995).

15 Frenkel, Y. I. On the behaviour of drops of liquid on the surface of a solid. I. Sliding of drops on an inclined plane. *J. Exp. Theor. Phys.* **18**, 658-667, (1948).

16 Kawasaki, K. Study of wettability of polymers by sliding of water drop. *J. Colloid Sci.* **15**, 402-407, (1960).

17 ElSherbini, A. & Jacobi, A. Retention forces and contact angles for critical liquid drops on non-horizontal surfaces. *J. Colloid Interface Sci.* **299**, 841-849, (2006).

18 Dussan, V. On the ability of drops to stick to surfaces of solids. Part 3. The influences of the motion of the surrounding fluid on dislodging drops. *J. Fluid Mech.* **174**, 381-397, (1987).

19 Wolfram, E. & Faust, R. in *Wetting, Spreading, and Adhesion* (ed J. F. Padday) 213 (Academic Press, 1978).

20 Antonini, C., Carmona, F. J., Pierce, E., Marengo, M. & Amirfazli, A. General Methodology for Evaluating the Adhesion Force of Drops and Bubbles on Solid Surfaces. *Langmuir* **25**, 6143-6154, (2009).

21 Berejnov, V. & Thorne, R. E. Effect of transient pinning on stability of drops sitting on an inclined plane. *Phys. Rev. E* **75**, 066308, (2007).

22 Tadmor, R. *et al.* Measurement of Lateral Adhesion Forces at the Interface between a Liquid Drop and a Substrate. *Phys. Rev. Lett.* **103**, 266101, (2009).

23 Timonen, J. V. I., Latikka, M., Ikkala, O. & Ras, R. H. A. Free-decay and resonant methods for investigating the fundamental limit of superhydrophobicity. *Nat. Commun.* **4**:2398 DOI: 10.1038/ncomms3398, (2013).

24 Lagubeau, G., Le Merrer, M., Clanet, C. & Quere, D. Leidenfrost on a ratchet. *Nat. Phys.* **7**, 395-398, (2011).

25 Pilat, D. W. *et al.* Dynamic Measurement of the Force Required to Move a Liquid Drop on a Solid Surface. *Langmuir* **28**, 16812-16820, (2012).

26 ’t Mannetje, D. *et al.* Electrically Tunable Wetting Defects Characterized by a Simple Capillary Force Sensor. *Langmuir* **29**, 9944-9949, (2013).

27 Olin, P., Lindström, S. B., Pettersson, T. & Wågberg, L. Water Drop Friction on Superhydrophobic Surfaces. *Langmuir* **29**, 9079-9089, (2013).

28 Pierce, E., Carmona, F. J. & Amirfazli, A. Understanding of sliding and contact angle results in tilted plate experiments. *Colloid Surf. A-Physicochem. Eng. Asp.* **323**, 73-82, (2008).

29 Sakai, M. *et al.* Direct Observation of Internal Fluidity in a Water Droplet during Sliding on Hydrophobic Surfaces. *Langmuir* **22**, 4906-4909, (2006).

30 Semprebon, C. & Brinkmann, M. On the onset of motion of sliding drops. *Soft Matter* **10**, 3325-3334, (2014).

31 Krumpfer, J. W. & McCarthy, T. J. Contact angle hysteresis: a different view and a trivial recipe for low hysteresis hydrophobic surfaces. *Farad. Discuss.* **146**, 103-111, (2010).

32 Griffiths, P. R. *Static and Dynamic Components of Droplet Friction* Master of Science in Mechanical Engineering thesis, University of South Florida, (2013).

33 Snoeijer, J. H. & Andreotti, B. Moving Contact Lines: Scales, Regimes, and Dynamical Transitions. *Annu. Rev. Fluid Mech.* **45**, 269-292, (2013).

34 Perrin, H., Lhermerout, R., Davitt, K., Rolley, E. & Andreotti, B. Defects at the Nanoscale Impact Contact Line Motion at all Scales. *Phys. Rev. Lett.* **116**, 184502, (2016).

35 Huang, K. & Szlufarska, I. Green-Kubo relation for friction at liquid-solid interfaces. *Phys. Rev. E* **89**, 032119, (2014).

36 Daniel, D., Timonen, J. V. I., Li, R., Velling, S. J. & Aizenberg, J. Oleoplaning droplets on lubricated surfaces. *Nat. Phys.* **advance online publication**, (2017).

37 Butt, H.-J. *et al.* Energy Dissipation of Moving Drops on Superhydrophobic and Superoleophobic Surfaces. *Langmuir* **33**, 107-116, (2017).

38 Israelachvili, J. N. *Intermolecular and Surface Forces*. (Elsevier Science, 2011).

39 Butt, H.-J. & Kappl, M. *Surface and Interfacial Forces*. (Wiley, 2010).

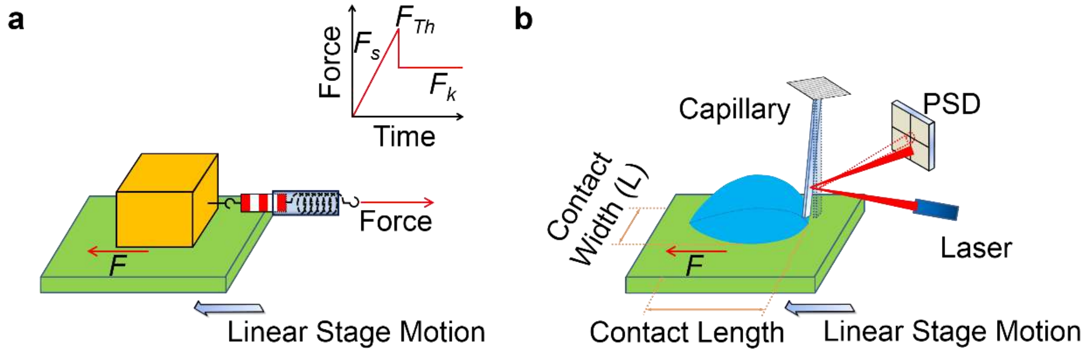

Figure 1| Schematics of friction force measurements. **a**, Textbook configuration for demonstrating solid–solid friction. **b**, Homemade setup for measuring liquid–solid friction. A drop of liquid is placed on a solid substrate mounted on a linear stage driven by a step motor. A laser beam incident on the capillary is reflected to a position-sensitive detector (PSD). The contact width between the drop of liquid and the solid surface (orthogonal to the direction of motion) and contact length (parallel to the direction of motion) are simultaneously monitored by cameras (not shown).

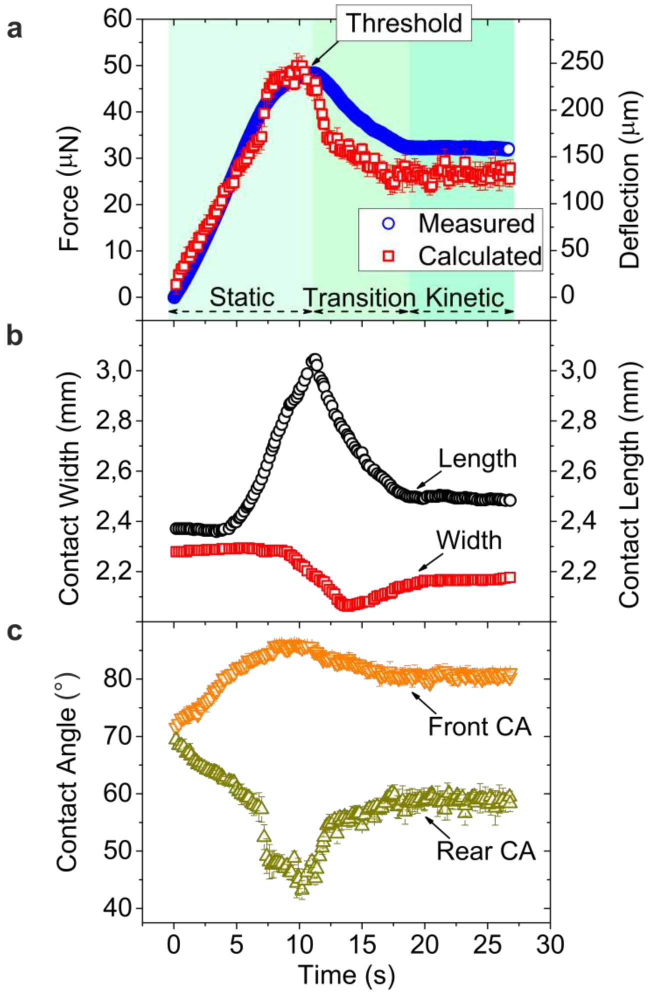

Figure 2| Lateral adhesion force experiment of a drop of ionic liquid (volume ≈1.5 μL) on a fluorinated Si wafer. The measurement was performed at a constant linear stage velocity of 200 μm/s. The surface tension of the ionic liquid 1-butyl-2,3-dimethylimidazolium bis(trifluoromethanesulfonyl)imide is 34.6 mN/m. **a**, The measured lateral adhesion force is plotted with blue circles. The error in force measurement is ±1 µN and smaller than the symbol size. The calculated force is plotted with red squares. **b**, Simultaneously determined contact width and length of the drop during the force measurement shown in **a**. **c**, Front and rear contact angles during the force measurement. Movie 1 shows the motion of the ionic liquid drop on the fluorinated Si wafer during the lateral adhesion force measurement.

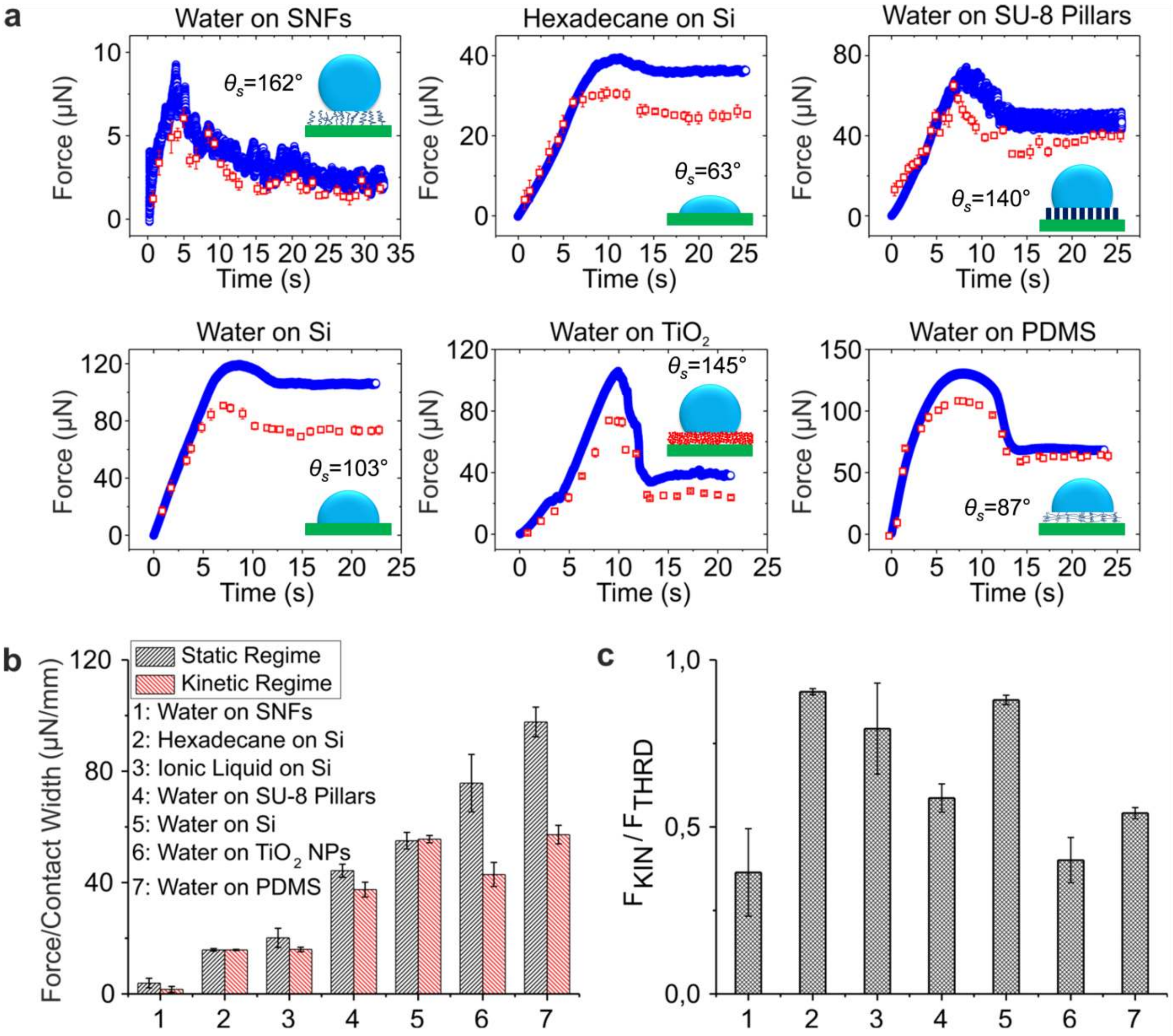

Figure 3| Lateral adhesion forces for drops of different liquids on solid surfaces. a, Measured (blue circles) and calculated lateral adhesion forces using k = 1 (red squares). The surfaces include silicone nanofilaments (SNFs), silicon wafers (Si), SU-8 square pillar arrays (height: 25 μm, width: 50 μm, centre–centre distance: 100 μm), multilayers of 20-nm titanium dioxide nanoparticles (TiO_2 NPs), and cross-linked polydimethylsiloxane (PDMS). All surfaces except for those of polydimethylsiloxane were fluorinated before use. All fabrication details are provided in the online methods section. The adopted surface tensions of water and hexadecane are 73.5 mN/m and 27.5 mN/m at room temperature, respectively. The advancing and receding contact angles were 171±1° and 164±1° for water on fluorinated silicone nanofilaments, 83±1° and 59±1° for hexadecane on fluorinated silicon wafers, 169±2° and 122±2° for water on fluorinated SU-8 pillars, 128±1° and 95±1° for water on fluorinated silicon wafers, 164±1° and 128±2° for water on titanium dioxide nanoparticles, and 121±1° and 81±1° for water on cross-linked PDMS, respectively (Supplementary Figs. 5–10). Movies 2–7 show the motions of drops on the different surfaces during the lateral adhesion force measurements. **b**, Lateral adhesion force per unit contact width. Drop volumes between 1.5 and 8 μL were chosen to avoid rupturing of drops during motion. **c**, Ratios of the kinetic friction force F_{KIN} and its threshold force F_{THRD} of all liquid–solid combinations that are studied. Here we used F_{KIN} and F_{THRD} prior normalization with the respective contact widths in order to point out $F_{\mathrm{KIN}}/F_{\mathrm{THRD}} \leq 1$. Error bars in b and c indicate variability between different experiments.

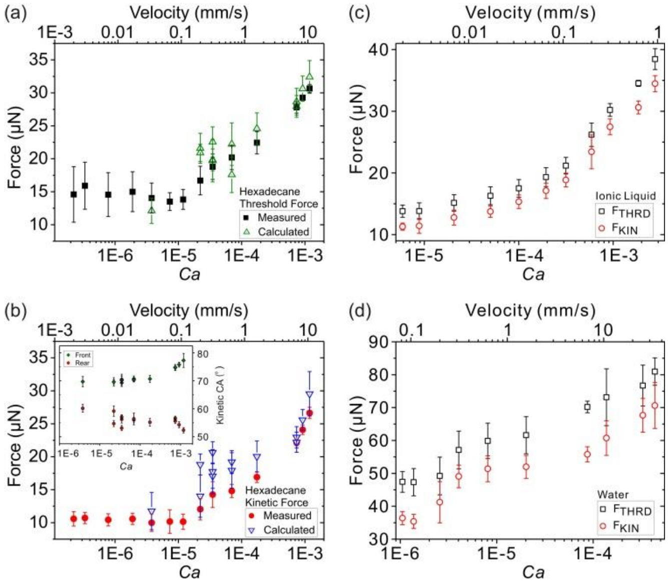

Figure 4| Velocity dependence of lateral adhesion forces. Development of the lateral adhesion force of hexadecane drops (≈ 3 µL) on a fluorinated Si wafer surface (a) at threshold and (b) in the kinetic regime. The inset shows the front and rear contact angles measured in the kinetic regime. (c) Velocity dependence of lateral adhesion forces of an ionic liquid (1-butyl-2,3-dimethylimidazolium bis(trifluoromethanesulfonyl)imide) drop (≈ 2 µL) on a fluorinated Si wafer substrate and (d) water drops (≈ 7.5 µL) on a fluorinated Si wafer substrate. Here velocities below 0.08 mm/s were not studied owing to evaporation of water. The error bars correspond to the standard deviation calculated from 5 - 7 independent measurements. The highest velocity that can be probed is given by the threshold force where the liquid drop detaches from the glass capillary (≈81 µN for water, ≈36 µN for ionic liquid and ≈31 µN for hexadecane).

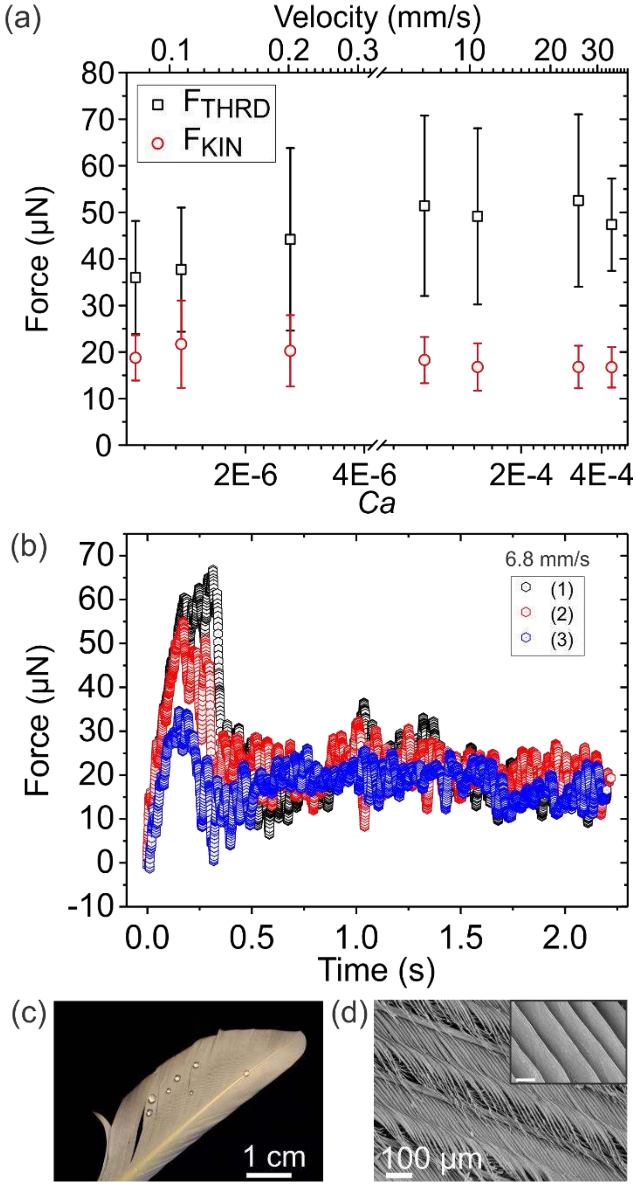

Figure 5| Lateral adhesion force measurement of a water drop on a goose feather (**a)** at threshold (black squares) and in the kinetic regime (red circles). The error bars correspond to the standard deviations calculated from 5 - 7 measurements each. **(b)** Three different lateral adhesion force measurement of a water drop on a goose feather at different areas at a velocity of 6.8 mm/s (drop volume of 8 μL). The threshold lateral adhesion force varied between 35 ± 1 µN and 67 ± 2 µN. Continuing the kinetic motion of the water drop required a force up to 35 µN. (**c)** An optical image of the feather with resting water drops. (**d)** Scanning electron microscopy images reveal the detailed structure of the feather. The inset is an enlarged area of (**c)** showing the microscopic structure. The scale bar in the inset is 10 μm.